 doi:10.20944/preprints202204.0018.v1

Suspended water droplet confined laser shock processing at elevated temperatures

Jian Liu [a], Xiaohan Zhang [a], Yali He [a], Zhe Zhao [a], Min Xia [b], Yaowu Hu [a*]

[a] *The Institute of Technological Sciences, Wuhan University, Wuhan, 430072, PR China*

[b] *Department of Engineering, Lancaster University, Lancaster, LA1 4YW, United Kingdom*

*Corresponding author: Yaowu Hu

E-mail: yaowuhu@whu.edu.cn

Abstract

The temperature-assisted laser shock process has shown promising prospects in the fields of forming manufacturing and surface strengthening. However, large-scale application of this process is limited by the instability and failure of confinement medium at high temperatures (≥300 ℃). Aiming at this problem, we propose a novel laser shock strategy based on Leidenfrost effect, where the suspended droplets are utilized as the confinement medium. According to the sequence of images acquired by time delay system and high-speed camera, the droplet dynamics behavior is studied. The focusing enhancement effect of the droplet is comprehensively explored. And the correlations between droplet size, ambient temperature, vapor layer thickness and focusing effect are investigated. Combining the dynamics and focusing enhancement effect of droplets, a theoretical model of laser shock pressure under droplet confinement is established. Finally, the effectiveness and feasibility of the droplet-based laser shock strategy in high temperature processing environments are verified by typical applications in laser shock forming and laser shock peening fields. The results show that the droplet-based laser shock process presents better forming effect. And the mechanical property tests demonstrate that this process can obtain the simultaneous improvement of the strength (~51%) and ductility (~6.4%) of annealed Cu. The multiscale plasticity mechanisms of the strengthened material are comprehensively investigated. We believe that this low-energy, low-cost and high-quality process can provide a new solution for the industrial application of laser shock at high temperatures.

Keywords: Droplet, Laser shock, High temperatures, Dynamics, Focusing enhancement

1. Introduction

During the past three decades, manufacturing processes based on laser shock (LS) effect have been under rapid development, driven by further fundamental understanding of mechanical shock wave effect in laser-matter interaction and increasingly advanced laser technologies. Among them, laser shock forming (LSF) and laser shock peening (LSP) are the two most representative applications of LS process. Applications of LSF span multiple scales from macroscopic thin-walled components [1] to nanostructure imprinting [2]. And LSP is considered to be an advanced technology that promises to replace traditional mechanical shot peening [3]. LS process has become a powerful tool in contemporary manufacturing field [4].

Typical application of LS technology in forming spans multiple scales, such as laser shock imprinting [5], laser shock flattening [6], and laser shock tuning [7], directly utilizing the controllable shape change produced by plastic deformation of metallic material. Laser shock imprinting can fabricate three-dimensional metallic structures with nanoscale precision in thin metal foils by generating ultrahigh-strain-rate deformations, and the resulting nano-patterns can be used in sensors and nano-devices [2]. Laser shock tuning based on collaborative superplastic flow is an

Preprints (www.preprints.org) | NOT PEER-REVIEWED | Posted: 4 April 2022 doi:10.20944/preprints202204.0018.v1

effective strategy for large-scale adjustment of nano-gaps in metallic nanostructures [8]. In addition to forming at room temperature, temperature-assisted LS process is of great interest for improving the plasticity, forming efficiency and forming quality of metals [9]. This is primarily attributed to the activation of special plastic mechanisms during thermoplastic deformation process, such as atomic diffusion or lattice boundary diffusion, which provide the possibility of superplastic forming of metals [10].

The evolution of the material's microscopic properties [11] and generation of surface compressive residual stress [12] caused by plastic deformation open up another avenue for the application of LS technology in metal or alloy strengthening. The significant contribution of LSP induced microstructure evolution is reflected in the change of strength and ductility of the material, while the residual stress significantly affects the fatigue properties of the materials [13]. The high-density dislocations, nano-twins and dynamic recrystallization caused by plastic deformation serve as fundamental mechanisms for the strengthening of metallic materials [14], while the LS-induced compressive residual stress is the core ingredient to inhibit the initiation and propagation of cracks during the fatigue process [15]. Additionally, compared with the room-temperature LSP technology, warm laser shock peening (WLSP) can significantly promote dynamic strain aging and dynamic precipitation behavior of metallic materials. The intense dislocation pinning effect and Orowan strengthening behavior can further improve the high-temperature microstructure stability and fatigue resistance [4,16]. Compared with the behavior in LSP implemented at room temperature, the strength of aluminum alloy 7075 processed using warm LSP process (250 ℃) is increased by ~32.3% without sacrificing ductility, which is attributed to nanoscale precipitate particles generated by WLSP and its dislocation blocking effect [17].

In view of applying LS in forming and strengthening, the introduction of temperature field can yield beneficial manufacturing effects. However, the rise of the ambient temperature during the LS process puts forward higher requirements on the high temperature stability and mechanical properties of the confinement layer, since that is considered to be the crucial medium that determine the shock pressure and shock effect [18]. At present, the commonly used confinement medium at room temperature mainly include transparent glass [19], silicone oil [16] and flowing water layer [20]. An unavoidable problem is that the high brittleness of glass leads to frequent breakage and low reutilization rate at high laser energy density (>4 $GW \cdot cm^{-2}$). This problem can be solved by replacing the glass with a water layer, but the application temperature of the water layer is believed to be limited to below 100 ℃. Silicone oil presents higher thermal stability and it is currently used in WLSP, but its stable operating temperature cannot exceed 300 ℃ and it is environmental unfriendly. Therefore, it is critical to develop suitable strategy to advance the application of laser shock in high temperature conditions for large-scale and green manufacturing.

In this paper, a novel high temperature LS strategy based on Leidenfrost phenomenon is proposed, where the water droplet is used as the confinement (WDC) layer. The dynamics of WDC in LS process is explored. Light field redistribution of the laser beam passing through the droplet is comprehensively studied. Based on the dynamic behavior and the focusing enhancement effect of droplet, the classical laser shock pressure calculation model is modified. Effectiveness of the droplet confinement strategy is verified by LSF and LSP of metal sheets, by characterizing the mechanical behavior and microstructure responses of the materials.

Preprints (www.preprints.org) | NOT PEER-REVIEWED | Posted: 4 April 2022 doi:10.20944/preprints202204.0018.v1

2. Experimental

2.1 Process Design

The schematic view of LS with WDC method is presented in Fig. 1(a). The deionized water droplets with radius (R_d) ranging from 1 to 3 mm were selected as the confinement medium. A metal needle was used to achieve droplet control, and the droplet control process is shown in Supplementary Video 1. All LS experiments in this study were carried out with temperature assistance, and the thermostatic platform was used as heat supply equipment to achieve the Leidenfrost phenomenon of liquid droplets. The temperatures range was set at 300 ℃ to 400 ℃. The Leidenfrost behavior at 300 ℃ are recorded by high-speed camera (Phantom-V1612), as shown in Fig.1 (b)-(d). It can be observed that the water droplet on thermostatic platform surface levitates over a film of vapor produced by its own evaporation. As a comparison, the classical LS process using glass as confinement layer was set (Fig. S1).

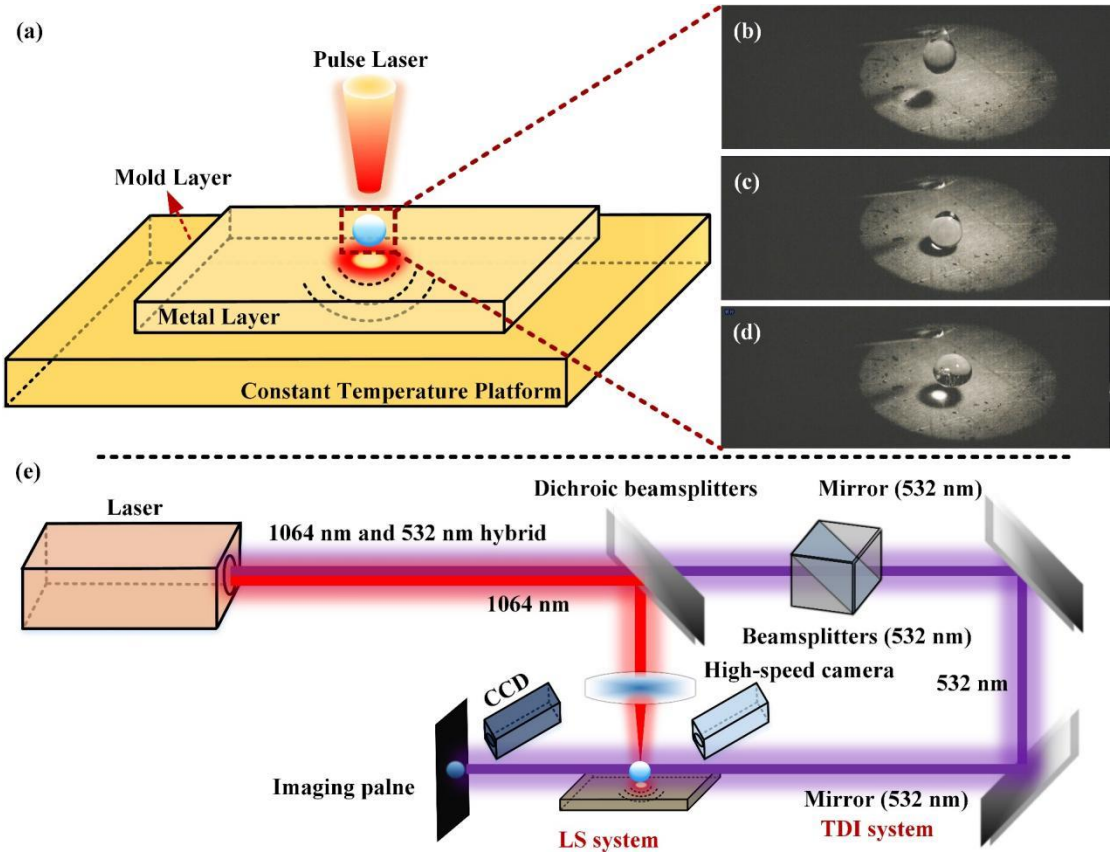

Fig. 1 The LS process with WDC: (a) Schematic view of LS with WDC, (b)-(d) High-speed camera images of droplet at 300 ℃, (e) Schematic diagram of optical path setup.

2.2 LSF and LSP experiments

Fig. 1(e) shows the optical path consisting of a LS system and a time-delay imaging (TDI) system in this study. Among them, the LS system was used to perform the LS process based on suspended droplets, and the TDI system was used to observe the dynamic behavior of the droplets at nanosecond scale. The filtering of the pulsed laser was achieved by dichroic beamsplitters. The pulsed laser with a wavelength of 532 nm was utilized as the light source for the TDI system, and the intensity of which was adjusted by a beamsplitter (532 nm). The dynamic behavior of droplets at the microsecond scale was captured by a high-speed camera.

Preprints (www.preprints.org) | NOT PEER-REVIEWED | Posted: 4 April 2022 doi:10.20944/preprints202204.0018.v1

In LSF experiments, Cu sheet with a thickness of 90 μm was selected as the target. The morphologies of the deformed region were measured by an optical surface profilometer (ZYGO-9000). The cross-sectional of the deformed region was observed by an optical microscope (OM), and the hardness of the deformed region was measured by a nanoindentation test. The laser pulse with a frequency of 1 Hz was offered by a pulsed solid-state laser (Nimma-900). Laser parameters are as follows: the laser energy of 800 mJ, the pulse duration of 7 ns, the wave-length of 1064 nm, and the focused spot radius of 1 mm. For the LSP experiment, copper or aluminum sheet with a thickness of 200 μm was used. The energy of the pulsed laser is increased to 1 J. The tensile experiments of the samples were performed by a mechanical testing machine (Instron-5956). The microstructure was observed by transmission electron microscopy (JEM-2100), and the TEM samples were prepared by argon ion thinning.

2.3 Simulation

To study the light field distribution, the droplet is equivalent to a spherical lens, and the simulations were repeated on sphere lens with different radius to ascertain the effect of water droplets on physical optical propagation of laser [21]. The optical path was designed according to the actual optical element placements, where a Gaussian light source with a wavelength of 1064 nm propagating through a focusing lens (THORLABS, BK7, LB1607), the suspending droplet, and the surface of the metal target sequentially. The parameters of the focal lens used in the experiment are as follows: curvature of ±179.1 mm^{-1}, thickness of 6.6 mm, focal length of 175 mm. The refractive index sphere lens was set to be 1.34. The location of the imaging plane is determined by the thickness of the vapor layer below the Leidenfrost droplet.

The dynamic deformation behavior of Cu sheet during LSF was characterized by finite element (FE) simulation based on ABAQUS platform. The LSF simulation is performed in a dynamic time step, and is assumed to be performed in an adiabatic environment. The shock wave is represented by a pressure load with a Gaussian distribution. The FE model consists of a mold and a Cu sheet, and the corresponding dimensions are shown in Fig. S2(a). The applied maximum load was derived from the calculation results of the theoretical model developed in this paper. The constitutive relation of Cu sheet was described by the widely accepted Johnson-Cook model [22], and the corresponding parameters are listed in Table S1.

The plasticity mechanism of the laser-induced nanograins at ultrahigh-strain-rate was verified by molecular dynamics (MD) simulations using large-scale atomic/molecular massively parallel simulator (LAMMPS) [23]. A polycrystalline model of Cu, which contains fifteen randomly oriented grains in a box of size of 40*20*10 nm, was used (Fig. S2(b)). The interactions of metallic atoms were described by the embedded-atom method (EAM) potential [24]. The model was first subjected to an energy minimization process by the conjugate gradient (CG) algorithm, followed by a relaxation of 60 ps under the NPT ensemble. The uniaxial tensile process along the x direction was carried out at a strain rate of 10E10 s^{-1}.

3. Results and Discussion

3.1 Dynamics behavior of droplet

3.1.1 Initial state of the droplet

The stable survival of droplets within the laser pulse duration is the precondition to implement confining process. The geometry of the droplets is captured by the high-speed camera, and are

Preprints (www.preprints.org) | NOT PEER-REVIEWED | Posted: 4 April 2022 doi:10.20944/preprints202204.0018.v1

plotted in Fig. 2(a). In the initial stage of Leidenfrost droplet formation, it is with slight fluctuation of the diameter (Fig. 2(b) and (c)), which is considered to be caused by the unstable flow of the vapor layer around the droplets. After ~400 ms, the droplet turns to a near-steady state, and is with a smooth surface (Fig. 2(d)). The evaporation and mass loss of the droplet are almost negligible within 1.6 s, which can fully satisfy the plasma confinement requirements on time scales from femtoseconds to milliseconds.

The processing temperature directly affects the initial state and quality of the droplet on the hot surface. The initial state of a droplet falling on the surface of target can be evaluated using two dimensionless numbers, which are defined as T^* and K, respectively [25].

$$T^* = \frac{T_s - T_b}{T_{Leid} - T_b} \tag{1}$$

$$K = \sqrt{\mathrm{We}} \cdot \mathrm{Re}^{0.25} \tag{2}$$

Where T_s is the temperature of target surface, T_b is the boiling point of water, T_{Leid} is the Leidenfrost temperature, We and Re represent the Weber number and Reynolds number, respectively. It can be found from Eq. (1) and (2) that T^* describes the temperature condition, and K represents the fluid dynamics of droplet. Based on the above conditions, the states of droplets falling on a high temperature surface can be classified into three regimes (Fig. 2(e)): deposition regime, splashing regime, and rebound regime. And, in this study, our experimental setup satisfies the boundary conditions of the rebound regime, where Leidenfrost droplets can form stably. In addition, the temperature loss of target caused by droplet forming is less than 1 °C, so the heat dissipation of the metal target during droplet confinement can be neglected [25].

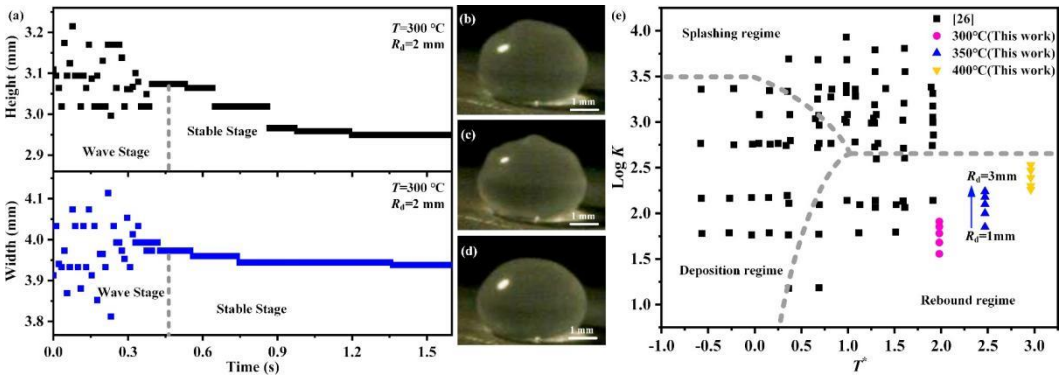

Fig. 2 The geometry of the droplet before the laser is turned on: (a) Droplet geometry versus time, (b)-(d) Series of time-resolved images of droplet at 0 ms, 0.22 ms, and 1.5 ms, respectively, (e) Droplet impingement regime mapping [26].

3.1.2 Time-dependent droplet behavior

In a typical laser shock process, two essential aspects are laser-induced plasma and plasma confinement. Single-pulse nanosecond laser-induced plasma and plasma escape processes at high temperatures are recorded in Fig. S3. It can be seen that when the laser is turned on, the laser-induced plasma is distributed in an approximate ellipsoid state in the air (Fig. S3(a)-(c)). This indicates that the plasma in the central area of the laser spot presents the highest velocity along the vertical direction. The subsequent expansion and escape processes of the plasma can be observed form Fig. S3(c)-(i), and the complete process lasts ~60 μs.

The nanosecond-scale dynamics behavior of droplets during LS process was captured by the TDI system (Fig. 3(a)-(f)). As can be seen from the series of images (Fig. 3(a)-(d)), the droplet does

Preprints (www.preprints.org) | NOT PEER-REVIEWED | Posted: 4 April 2022 doi:10.20944/preprints202204.0018.v1

not undergo significant global deformation behavior within the first 50 ns. The escape behavior of a small amount of ultrafast plasma can be observed at ~120 ns (Fig. 3(f)). The interaction between the droplet and the ultrafast plasma in the central region of the laser spot is simulated by MD (Supplementary Video 2). Fig. 3(g)-(j) presents a series of images revealing the motion of ultrafast plasma in the droplet. The plasma impinging into the droplet does not directly induce the explosion or severe deformation of the droplet (Fig. 3(g) and (h)), which is consistent with the results observed in the TDI system. The ultrafast movement of the plasma inside the droplet drives the movement of water molecules around the path together, creating a hollow channel (Fig. 3(i)). And the bottom of the channel can be refilled by water molecules. Finally, the escape of the ultrafast plasma is observed in the top region of the droplet (Fig. 3(j)).

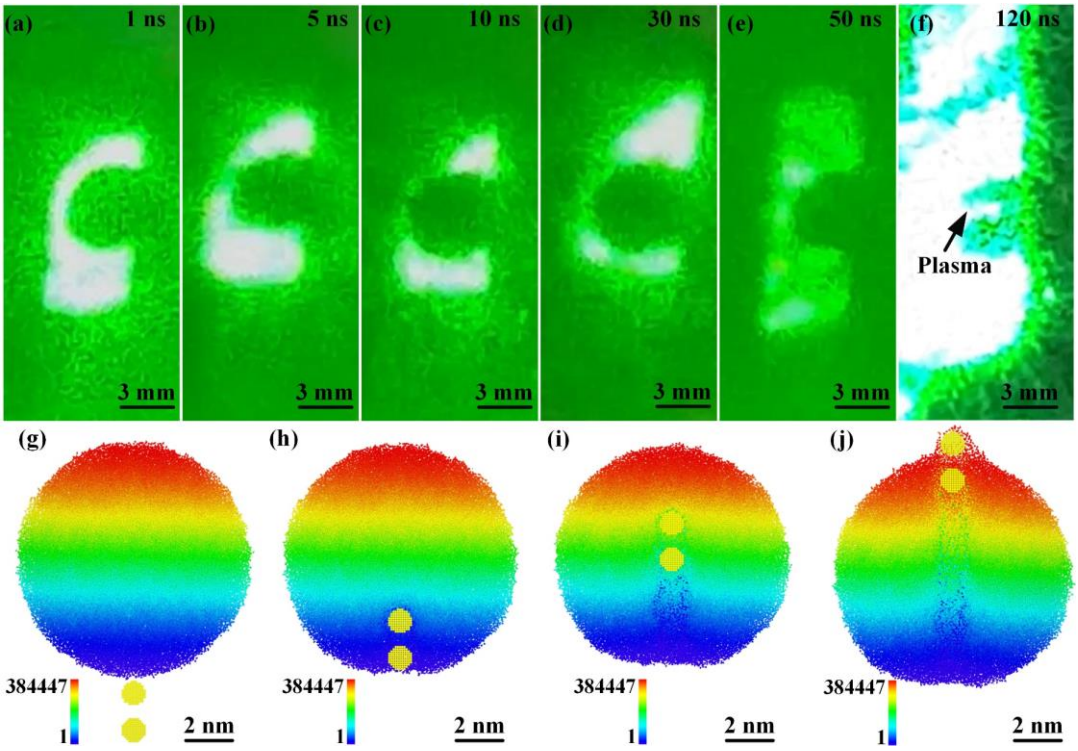

Fig. 3 Dynamics behavior of droplets at the nanosecond scale in LS process: (a)-(f) Series of time-delayed images of droplet, (g)-(j) Series of MD results revealing ultrafast plasma-droplet interactions (Colored by particle identifier).

A series of images in Fig. 4 presents the microseconds-scale dynamics behavior of the droplet. The dynamic behaviors, including initial state (Fig. 4(a)), laser-induced plasma (Fig. 4(b) and (c)), plasma confinement (Fig. 4(d)-(i)), and explosion (Fig. 4(j)-(m)) processes, are integrally recorded (Supplementary Video 3). It should note that only a small range of plasma escape behavior can be observed, implying that the droplets have qualified plasma confinement capabilities. Additionally, in the WDC-based LS process, multiple physical phenomena including laser-induced plasma, laser-induced bubble, bubble collapse shock wave, shock wave emission, and laser-induced counterjet can be observed. According to the dynamic evolution behaviors of droplet shown in Fig. 4, the physical phenomenon of the whole process can be described in three categories.

(1) The first phenomenon can be summarized as laser-induced bubble process. When the droplet is initially irradiated by the nanosecond laser, the droplet is broken down and plasma is formed inside the droplet, as shown in Fig. 4(b). The plasma in the droplet expands and forms plentiful bubbles. And the bubbles are mainly located on the free surface above the equatorial plane

Preprints (www.preprints.org) | NOT PEER-REVIEWED | Posted: 4 April 2022 doi:10.20944/preprints202204.0018.v1

due to the effect of surface tension (Fig. 4(c)). The surface pulsating shock wave generated by the collapse of the droplet can be seen in Fig. 4(d) and (e).

(2) This extremely important process can be described as a laser-induced plasma process on the surface of metallic target. The transparent water droplet has a significant focusing enhancement effect, equivalent to placing a flexible lens on the near surface of targets [27], which will be discussed in following section. The pulsed laser light focused by the droplet propagates to the metal surface, and the classical laser-induced plasma process occurs. A small amount of plasma escape can be found in the central region of laser irradiation (Fig. 4(b)). And plasma residues on the metal surface can be observed in Fig. 4(c) and (d).

(3) The final phenomenon is the explosion of droplet (Fig. 4(c)-(m)). The vertical motion of the high-temperature plasma in the central region of the laser irradiation promotes the ejection of the counter-jet [28]. Further, the confinement of the droplet to the laser-induced plasma results in the explosion, fragmentation and splashing behavior, as evidenced by the preferential splashing at the bottom of the droplet. In addition, the study results of the laser-generated bubble dynamics demonstrated that the collapse of the bubble in the bottom region of the droplet would lead to the generation of the micro-jet [29]. As shown in Fig. 3(d), the significant splashing effect is first observed from the bottom of the droplet, followed by the upward propagation of the plasma shock wave in the vertical direction (Fig. 4(d)-(i)). Finally, the droplets are completely dispersed in the air (Fig. 4(j)-(m)), and no significant liquid residue was observed on the metallic surface.

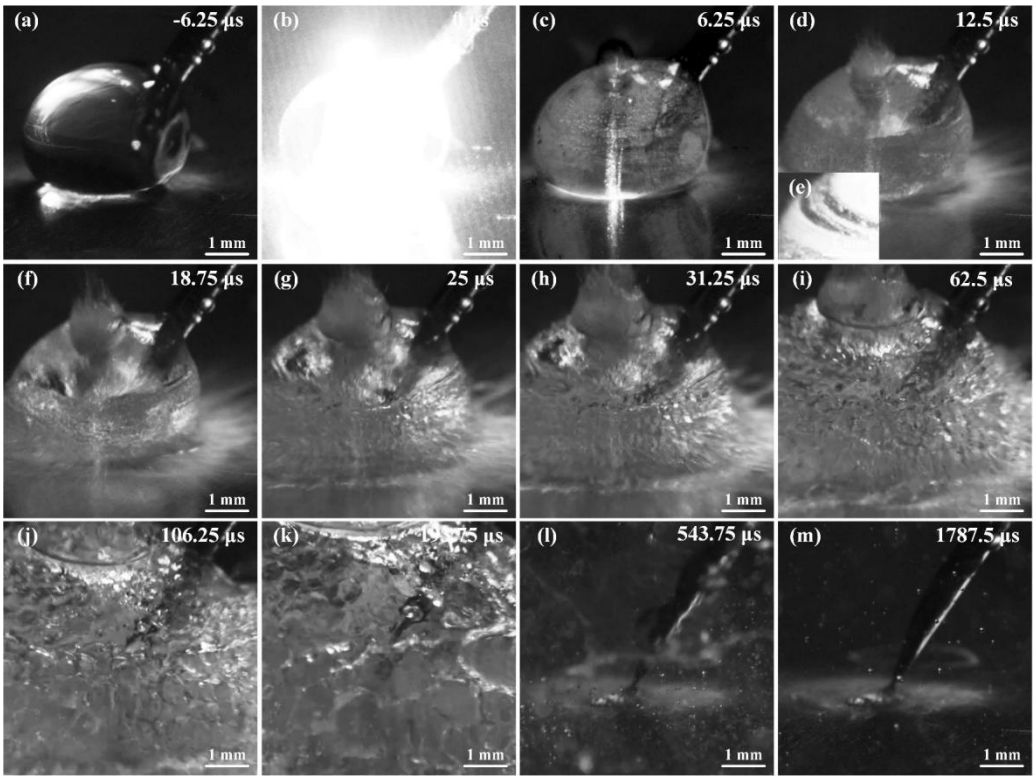

Fig. 4 Series of time-resolved images of droplet (R_d=2 mm) in LS process: (a) -6.25 μs, (b) 0 μs, (c) 6.25 μs, (d) 12.5 μs, (e) Enlarged view of pulsating shock wave, (f) 18.75 μs, (g) 25 μs, (h) 31.25 μs, (i) 62.5 μs, (j) 106.25 μs, (k) 193.75 μs, (l) 543.75 μs, (m) 1787.5 μs.

3.2 Focusing enhancement of droplet

3.2.1 Focusing enhancement effect

Different from the traditional LS process, the laser undergoes an additional focusing process

Preprints (www.preprints.org) | NOT PEER-REVIEWED | Posted: 4 April 2022 doi:10.20944/preprints202204.0018.v1

by the droplet in the LS process with WDC. The droplet acts as a liquid lens appreciated by the spherical morphology and transparent characteristic of the droplet. The focusing effect of the droplet was characterized by laser ablation of the metal surface, as shown in Fig. 5(a)-(d). When the surface was directly irradiated by the pulsed laser, the radius of the ablated area (Fig.5 (a)) is ~ 767.4 μm. The focusing enhancement effect of the droplet can be demonstrated by the significantly reduced ablation area in Fig. 5(b)-(d). When the laser is refocused by droplets with radii of 1 mm, 1.5 mm, and 2 mm, the resulting ablated regions present radii of 198.2 μm, 402.8 μm, and 592.4 μm, respectively. Additionally, the physical propagation behaviors of laser Gaussian beam in different confinement cases were simulated to testify the focusing enhancement effect of droplets. We take the focusing lens (THORLABS, BK7, LB1607) as an example. For the optical lens, the required focusing distance is about 7.7 mm to focus a beam with a radius of 1 mm to 205 μm, while this can be achieved in 2.02 mm (Droplet sizes (R_d=1 mm) are included) by using droplet lens. It can be found from Fig. 5(e), the glass (Thickness=2 mm) confinement exhibits negligible effect on laser propagation, and the difference in the radiation intensity distribution along the radial direction (Fig. 5(g)) is nearly consistent with the case without the confining medium. In addition, the obvious focusing enhancement of light spatial distribution can be observed when the laser passes through the droplet (R_d=1 mm), as shown in Fig. 5(f). The droplet acts as a high curvature droplet lens, and the theoretical irradiation intensity reaching the metal target surface is 7.6 times of that for glass confinement (Fig. 5(g)).

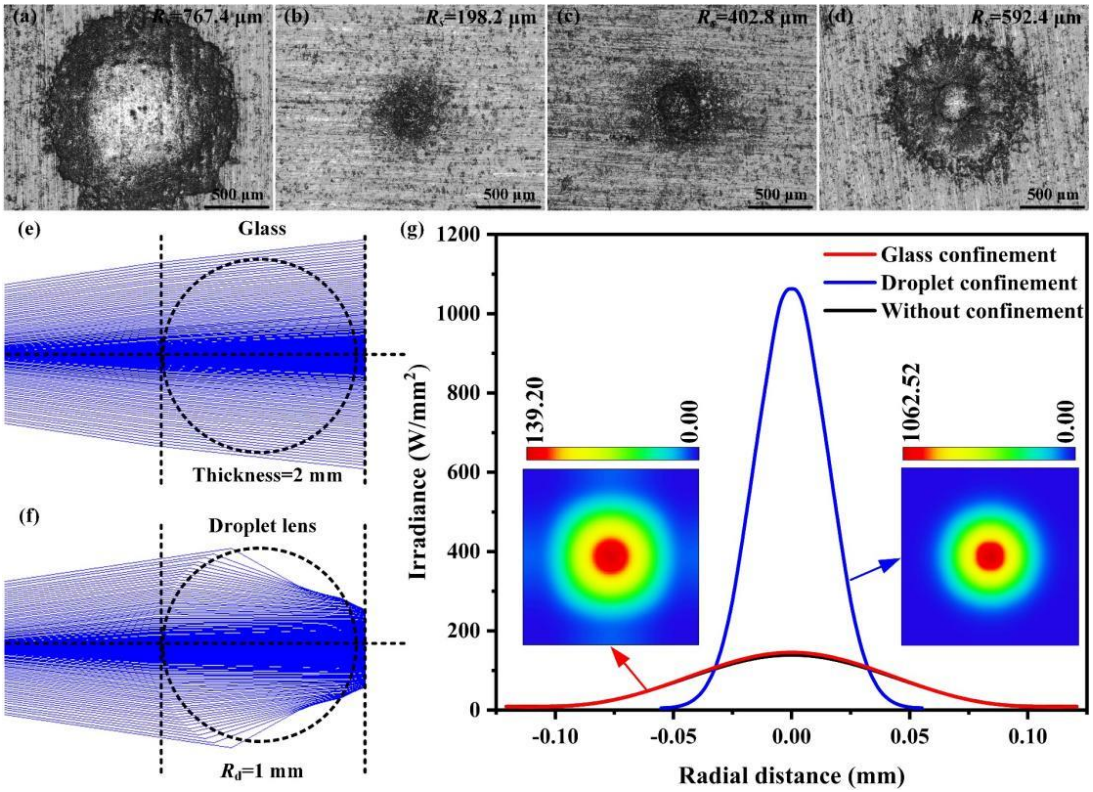

Fig. 5 Simulation results on the physical-optical propagation of laser beam: (a) Metallographic image of laser ablated region with glass confinement, (b)-(d) Metallographic image of laser ablated region with WDC (R_w=1 mm, 1.5 mm, and 2 mm, respectively), (e) Physical-optical propagation of laser with glass confinement, (f) Physical-optical propagation of laser with WDC (R_w=1 mm), (g) Plot of the beam irradiance intensity versus axial distance.

Regarding the influence of droplet size on focusing enhancement behavior, we considered the

Preprints (www.preprints.org) | NOT PEER-REVIEWED | Posted: 4 April 2022 doi:10.20944/preprints202204.0018.v1

effect of the thickness of the vapor layer (e) below the droplet on focusing behavior as well, because the thickness of the vapor layer determines the imaging distance. The thickness of the vapor layer is dominated by the droplet size and temperature, which can be described by Biance's model [30]. And the vapor thickness is given as:

$$e = \left(\frac{3\kappa\Delta T\eta}{4L\rho_v\rho g a}\right)^{1/4} R_w^{1/2} \tag{3}$$

where e represents the vapor layer thickness, κ the thermal conductivity, ΔT the different between the target temperature and the boiling temperature of the water, η the dynamic viscosity, L the latent heat, ρ_v the vapor density, ρ the water density, g the gravitational acceleration, a the capillary length ($a=(\gamma/\rho g)^{1/2}$, denoting the liquid surface tension and density as γ and ρ), and R_w the droplet radius. The above parameters used in this study are listed in Table S2, and the corresponding calculation results are plotted in Fig. 6(a). It can be observed that the increase of temperature promotes the thickening of the vapor layer, and the thickness of the vapor layer tends to expand linearly with the expansion of the droplet. The contribution of temperature to the thickness of the water vapor layer progressively increases with the droplet's growth. By approximating the calculated results of the vapor layer thickness to the imaging distance between the metal target and the droplet, we simulate the systematic values of the spot size on the target surface (Fig. 6(b)). The focus enhancement effect of the droplet is fitted by an exponential function:

$$R_s = 920.4\exp\left(-\frac{1}{R_w - 0.3}\right) \tag{4}$$

It can be found from Fig. 6(b) and Eq. (4) that the vapor layer thickness exhibits a tiny effect on the laser spot. And the focusing enhancement effect is primarily dominated by the droplet size which determines the curvature of the liquid lens. Therefore, the effect of temperature on the spot size is ignored in the nonlinear fitting process.

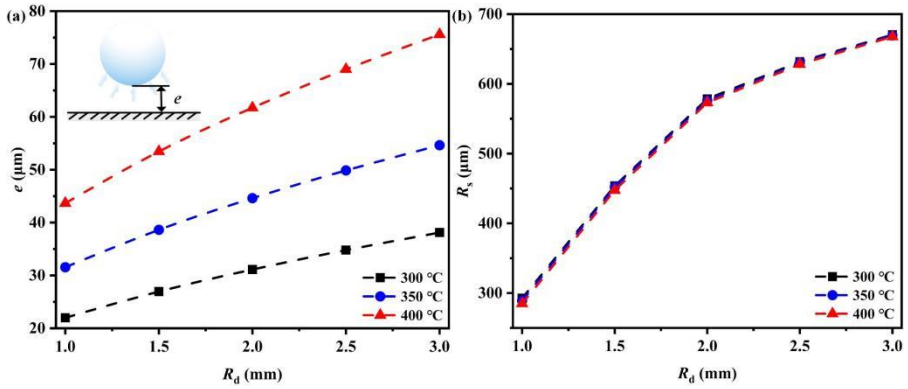

Fig. 6 Theoretical calculation results of vapor layer thickness and spot size.

3.2.2 Model of laser shock pressure

Based on the dynamic analysis of droplet in the previous section, it can be concluded that the sources that may provide the shock pressure in the droplet confinement laser shock process include laser-induced shock pressure (P_{ls}), bubble collapse shock wave (P_{bc}), and liquid micro-jet (P_{jet}), as shown in Fig. 7(a). These physical phenomena appear to be similar to those in the laser cavitation peening process [31,32], which uses water layer as the confinement medium at room temperature. However, there is a radical difference in the dominant mechanism of the laser shock pressure due to the distinct difference in the bubble dynamics between water layer and droplet. The existence of the vapor layer between the droplet and high temperature surface avoids the direct contact of materials,

Preprints (www.preprints.org) | NOT PEER-REVIEWED | Posted: 4 April 2022 doi:10.20944/preprints202204.0018.v1

while it is a gapless contact between the water layer and the target surface at room temperature. The various interface states lead to different kinetic behaviors of laser-induced bubbles, where bubbles in droplets tend to move toward the free surface above the equatorial plane, and bubbles in water layers are preferentially adsorbed toward the surface of target. Therefore, the primary source of shock pressure in laser cavitation shock is the collapse of the bubbles, and the released shock pressure is up to GPa level [33], which are attributed to the collapse behavior occurring near the target surface (Fig. 7(b)). Conversely, the bubble collapse in this study mainly occurs at the top area of the droplet (Fig. 4(c)), and bubble collapse shock wave cannot propagate to the target surface on the nanosecond time scale and the millimeter distance scale.

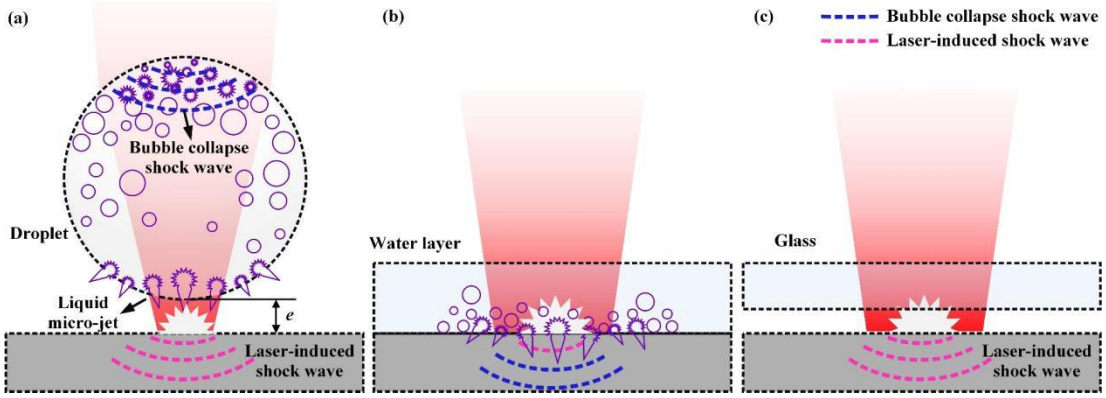

Fig. 7 Schematic diagram of the laser shock pressure model under different confinement strategies: (a) Droplet, (b) Water layer, (c) Glass.

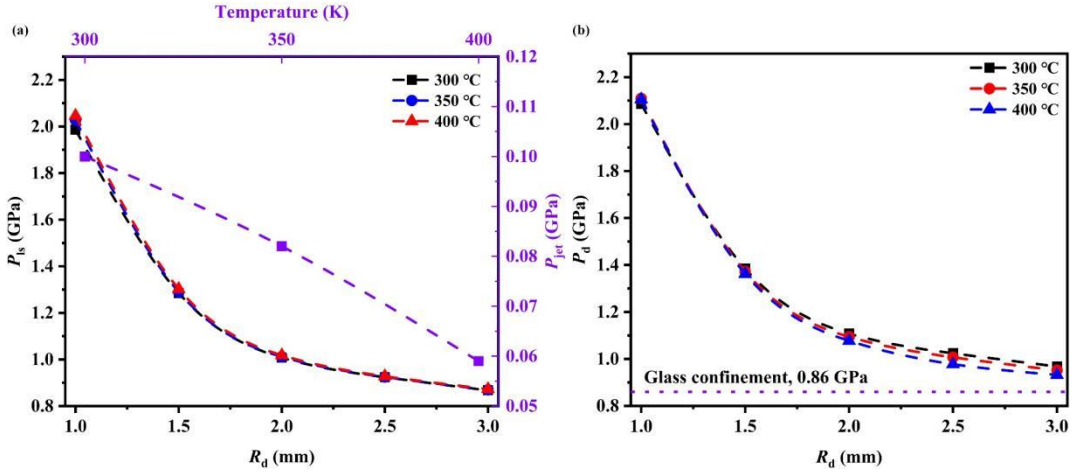

Fig. 8 The calculated results of the theoretical pressure: (a) P_{ls} and P_{jet} for droplet enhancement, (b) P_d for droplet and glass confinement.

The shock pressure induced by the micro-jet (P_{jet}) can be described by the water hammer effect, which can be expressed as [34]:

$$P_{jet} = \frac{\rho_1 \rho_2 c_1 c_2}{\rho_1 c_1 + \rho_2 c_2} V_{jet} \tag{5}$$

where ρ_1, ρ_2 and c_1, c_2 are the densities and sound speed of materials, and V_{jet} is the velocity of the micro-jet. In the case of solid confinement medium, only laser-induced shock pressure exists (Fig. 7(c)). And according to Fabbro et al [35,36] , the P_{ls} is given as:

$$P_{ls} = 0.01\left(\frac{\alpha}{2\alpha + 3}\right)^{1/2} Z^{1/2} I^{1/2} \tag{6}$$

Preprints (www.preprints.org) | NOT PEER-REVIEWED | Posted: 4 April 2022 doi:10.20944/preprints202204.0018.v1

where α is a constant fraction of the internal energy and represents the thermal energy, Z the shock impedance ($2/Z=1/Z_1+1/Z_2$, denoting the shock impedance of target material and confinement material as Z_1 and Z_2, respectively), and I is the laser power density ($I=E/S\cdot\tau$, where E is laser energy, S is the spot area, and τ is the pulse width). Therefore, the generalized shock pressures in the case of water layer (P_{wl}), droplet (P_d) and glass (P_g) confinement can be expressed as follows:

$$P_{wl} = P_{bc} + P_{jet} + P_{ls} \tag{7}$$

$$P_{d} = P_{jet} + P_{ls} \tag{8}$$

$$P_{g} = P_{ls} \tag{9}$$

Considering the focusing improvement effect of the droplet, the laser shock pressure in the case of droplet confinement can be obtained by coupling Eqs. (4), (5) and (8).

$$P_{d} = \frac{\rho_1\rho_2 c_1 c_2}{\rho_1 c_1 + \rho_2 c_2} V_{jet} + 92.04 \exp\left(-\frac{1}{R_d - 0.3}\right)\left(\frac{\alpha}{2\alpha+3}\right)^{1/2} Z^{1/2}\left(\frac{E}{\pi\tau}\right)^{1/2} \tag{10}$$

The calculated results of the theoretical shock pressure are plotted in Fig. 8, and the parameters used are provided in Tables S2 and S3. Compared with the effect of processing temperature, the laser-induced shock pressure shows a significant size-dependence behavior (Fig. 8(a)), which is consistent with the correlation between vapor layer thickness and spot size. In addition, the micro-jet pressure exhibits a strong temperature-dependent effect attributed to the change in liquid density. It should be noted that from Fig. 8(b), by using the droplet confinement strategy, the shock pressure is maximally increased by ~2.4 times compared with that of glass confinement.

3.3 Application validation

3.3.1 Metal sheet forming using laser shock with droplet confinement

Fig. 9 shows the deformed geometries of the Cu sheets processed by LSF with different confinement strategies at 300 ℃. The measured results at higher processing temperature (350 ℃ and 400 ℃) are presented in Fig. S4. The Cu sheet presents limited deformation area and plastic strain under glass confinement (Fig. 9(a)). Conversely, when the glass is replaced with droplets, significantly increased plastic strain can be observed in Fig. 9(b). And the center of the forming region exhibits more concentrated plastic deformation, benefiting from the focusing enhancement effect of the droplet (Fig. 9(i)). The deformation depth in the vertical direction decreases with the increase of the droplet size (Fig. 9(b)-(d)), which indirectly verifies the statement of the size-dependent effect of the shock pressure. The systematic values of forming depth are plotted in Fig. 9(j). The droplet confinement strategy shows significant advantages in LSF field, and the effect of temperature on forming depth can be explained by the thermos-plasticity of the metal. Also, the center of the forming region still maintains satisfactory thickness uniformity, as evidenced by the cross-sectional metallographic images in Fig. 5(e-h). The application process of laser shock technology based on droplet confinement strategy in forming is also verified by finite element simulations (Fig. S5) with theoretical calculation results (Fig. 8(b)) of the shock pressure applied. The characteristics of the forming region are in good agreement with the experimental results, which verifies the correctness of the theoretical model (Eq. (9)) of the shock pressure in this study. These forming morphology analysis results demonstrate that the laser shock forming technology based on droplet confinement can improve the forming quality and forming efficiency.

The mechanical properties of the forming region were characterized by nanoindentation, as

Preprints (www.preprints.org) | NOT PEER-REVIEWED | Posted: 4 April 2022 doi:10.20944/preprints202204.0018.v1

shown in Fig. 10. The loading-unloading curves in Fig. 10(a) indicate that the droplet confinement strategy shows a better surface hardness improvement effect. The surface hardness of the forming regions is 1.54 GPa (R_d=1 mm), 1.51 GPa (R_d=2 mm), 1.48 GPa (R_d=3 mm), 1.47 GPa (Glass), respectively. Additionally, the hardness distribution along the cross-sectional direction of the forming region is counted in Fig. 10(b). With benefits from the droplet confinement strategy, a significant increase in hardness along the depth direction can be observed, which suggests the affected depth of the laser shock pressure under the droplet confinement layer. Furthermore, the hardness decay along the depth direction is visibly weakened, and the variance of hardness distribution along the depth direction can be reduced up to 4 times.

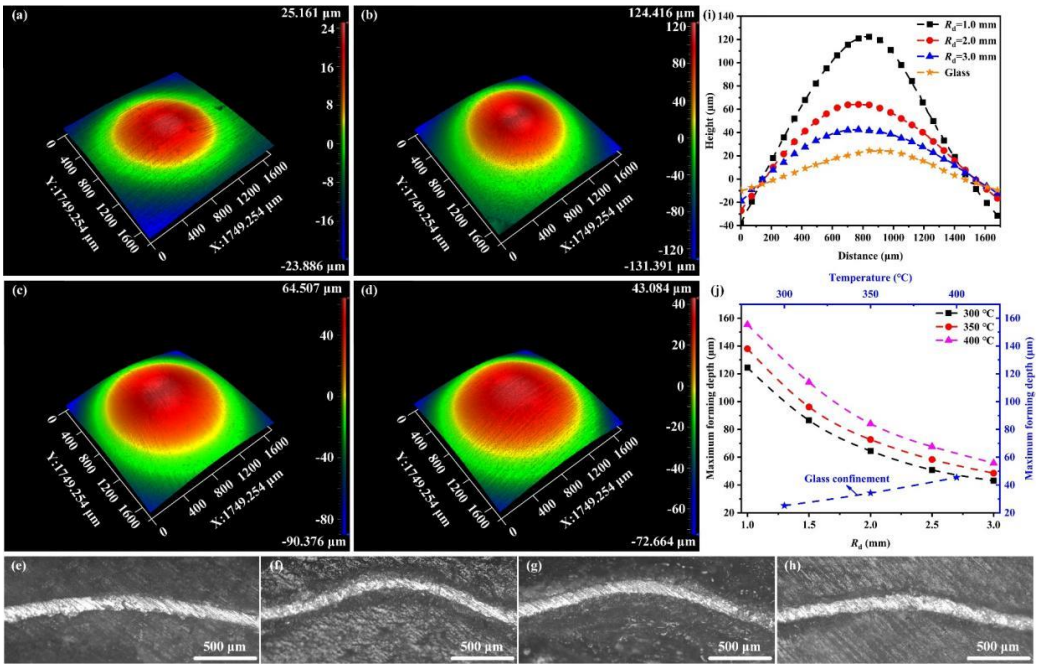

Fig. 9 Surface and cross-sectional morphologies of Cu sheets processed by LSF with different confinement methods: (a) 3D morphology of Cu sheet LSFed with glass confinement, (b-d) 3D morphologies of Cu sheet LSFed with WDC (R_d=1 mm, 2 mm, and 3 mm, respectively), (e) Cross-sectional metallographic images of Cu sheets LSFed with glass confinement, (f)-(h) Cross-sectional metallographic images of Cu sheets LSFed with WDC (R_d=1 mm, 2 mm, and 3 mm, respectively) (i) 2D profiles, (j) Maximum forming depth curves.

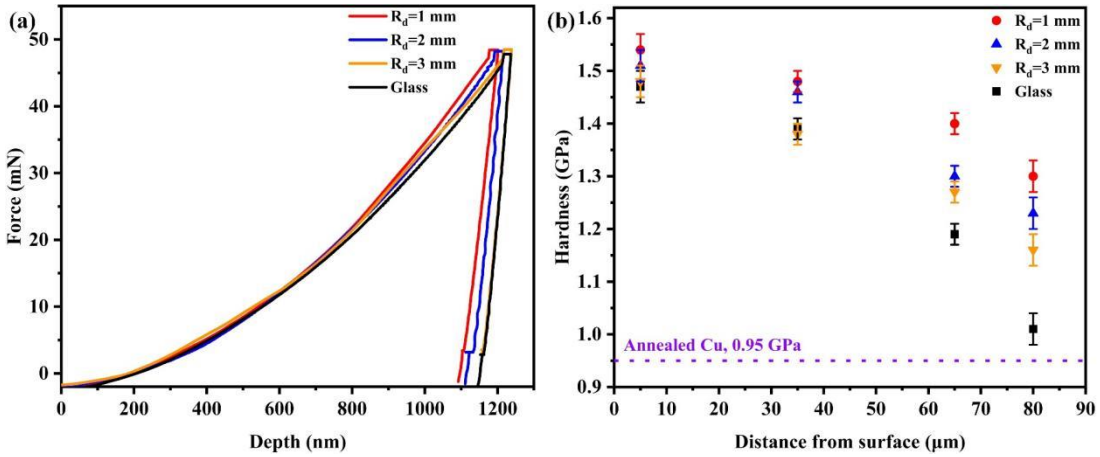

Fig. 10 Nanoindentation results of the deformed Cu sheets: (a) Nanoindentation curves of Cu surfaces formed with different confinement strategies, (b) Cross-sectional hardness distribution of

Preprints (www.preprints.org) | NOT PEER-REVIEWED | Posted: 4 April 2022 doi:10.20944/preprints202204.0018.v1

Cu sheets with different confinement strategies.

3.3.2 Laser shock peening with droplet confinement

To demonstrate the potential application of droplet confinement-based laser shock strategy for metal strengthening in high temperature environments, tensile tests of Cu samples after annealing and laser shock peening with droplet confinement at 300 ℃ were performed. Due to the fragility of glass under high temperature environment and continuous shock process (Fig. S6), the preparation of peened samples using glass confinement was not successful. From the stress-strain curve in Fig. 11, it can be observed that the strength and ductility of the LSPed Cu sheet with WDC are significantly improved simultaneously. The annealed Cu shows the 0.2% yield strength of ~43 MPa, and the ultimate tensile strength of ~234.4 MPa with the uniform elongation of ~45.3%. The LSPed Cu sheet, however, exhibits a ~51% increase in yield strength (~65.2 MPa), a ~13.4% elevation in ultimate tensile strength (266.1 MPa), and a ~6.4% increase in uniform deformation elongation (51.7%). We consider that this dual improvement in mechanical properties is closely related to the LSP-induced evolution of microstructure and crystal defects.

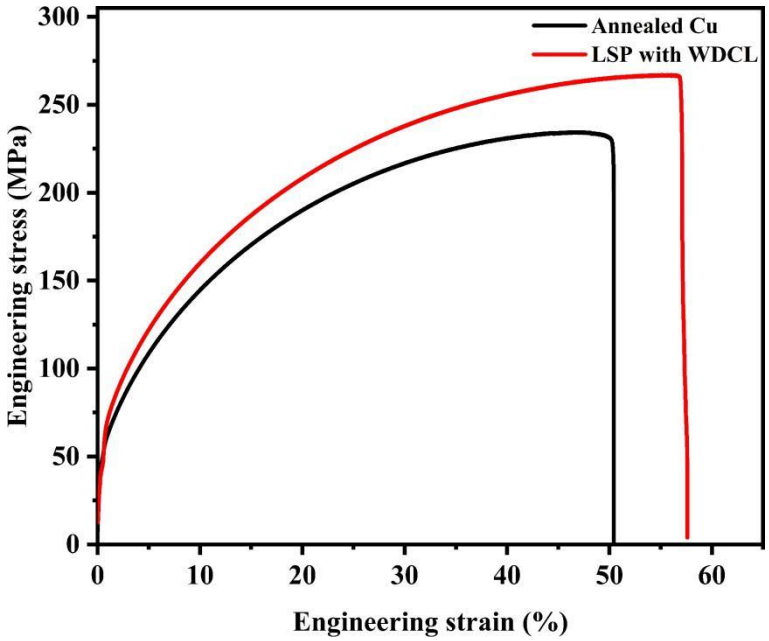

Fig. 11 Engineering stress-strain curves of annealed Cu (black line) and LSPed Cu with WDC. (R_d=2 mm, red line).

The microstructure and plastic mechanism of annealed Cu sheet is analyzed. Fig.12(a) presents the OM image of the annealed Cu at 300 ℃. It can be found that the annealed Cu consists of micron-scale coarse grains (CGs) with annealing twins (ATs) generated by recrystallization. The plasticity mechanism of annealed Cu is characterized by TEM observation of the deformed sample. Typical defects caused by plastic deformation, including high-density dislocation walls (DWs), dislocation cells (DCs), and dislocation tangles (DTs), can be observed in Fig. 12(b). Further, interactions between dislocations and ATs can be observed in Fig. 12(c). The slippage of numerous dislocations is prevented by the boundary of ATs, and high-density DTs can be found around the twin boundaries. Therefore, it can be drawn that the strain of annealed Cu is borne by the CGs and the plasticity mechanism is mediated by dislocations.

The microstructure of the Cu sheet processed by LPS with WDC strategy at 300 ℃ is shown in Fig. 13. Gradient grains, consisting of ultrafine grains (UFGs) and nanograins (NGs), can be

Preprints (www.preprints.org) | NOT PEER-REVIEWED | Posted: 4 April 2022 doi:10.20944/preprints202204.0018.v1

found in the near-surface region of the sample (Fig. 13(a)). And with further extension, a NGs/CGs gradient structure can be observed (Fig. 13(b)). The enlarged views of NGs and DCs are shown in Fig. 13(c) and (d), respectively. The DCs can be found within the NGs region. Unlike the DCs in the annealed Cu, the DCs in NGs consist of high-density nanotwins (NTs), as evidenced by the SAED result in Fig. 13(e). Furthermore, the UFGs are almost defect-free (Fig. 13(d)), and the excellent crystallinity can be confirmed by the SAED result in Fig. 13(f). The statistical results of the grain size manifest that the average grain size of the UFGs (Fig. 13(g)) and NGs (Fig. 13(h)) is 9±2.67 nm and 48±15.7 nm, respectively. The above results demonstrate that the LSP process based on WDC can achieve effective grain refinement at high temperatures, and can induce a gradient grain structure along the shock wave dissipation direction.

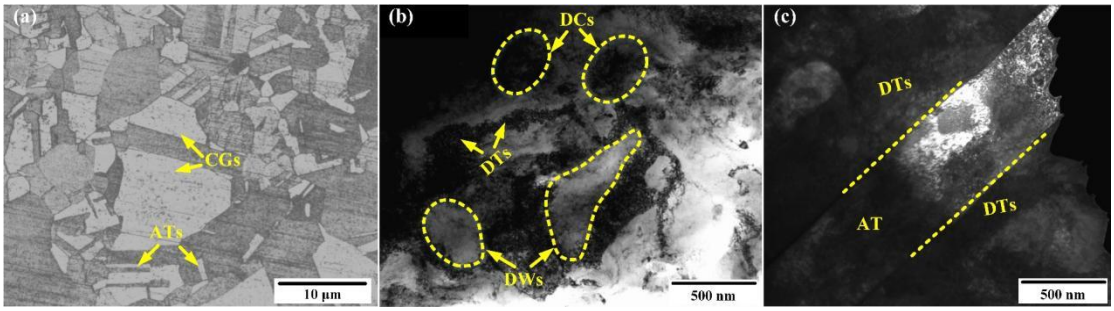

Fig. 12 Microstructure and plastic mechanism of annealed Cu: (a) OM image of annealed Cu, (b) and (c) TEM images of deformed Cu.

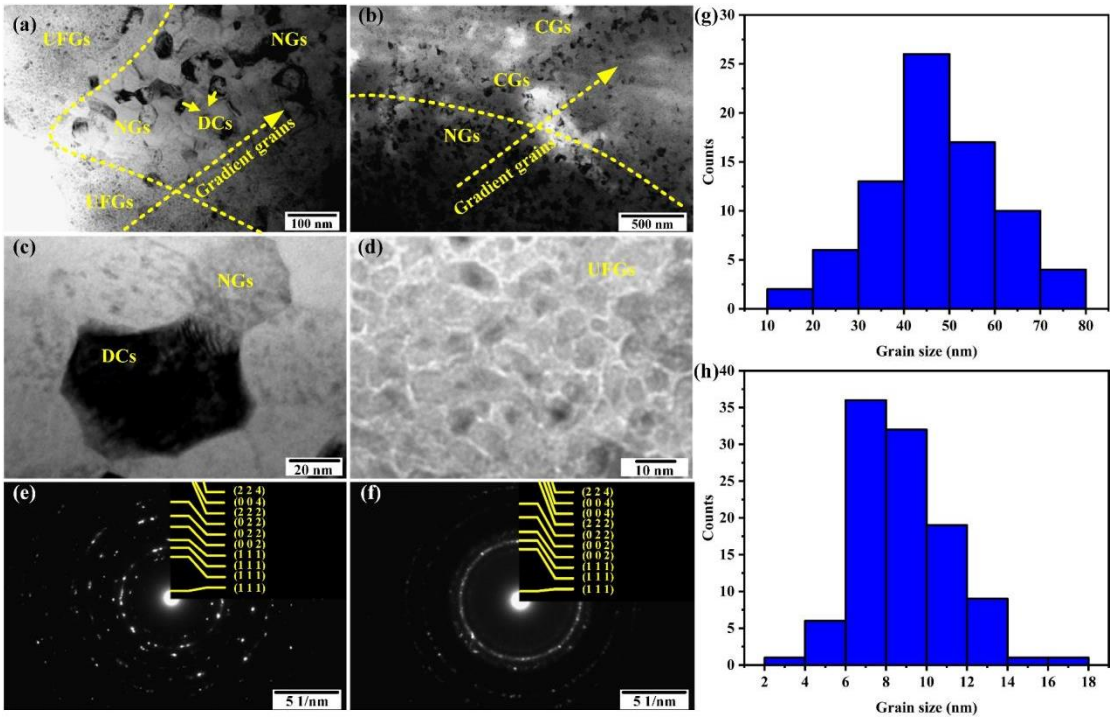

Fig. 13 TEM results of LSPed Cu sheets with WDC: (a) TEM image of UFGs/NGs gradient grains of Cu sheets processed by LSP with WDC (R_d= 2 mm) at 300 °C, (b) TEM image of NGs/CGs gradient grains of Cu sheets processed by LSP with WDC (R_d= 2 mm) at 300 °C, (c) Enlarged view of NGs, (d) Enlarged view of UFGs, (e) SAED results of NGs, (f) SAED results of UFGs, (g) Statistical results of UFGs size, (h) Statistical results of NGs size.

We further explore the deformation mechanism of UFGs and NGs by HRTEM, as shown in

Preprints (www.preprints.org) | NOT PEER-REVIEWED | Posted: 4 April 2022 doi:10.20944/preprints202204.0018.v1

Fig. 14. Unlike to the dislocation-accommodated plastic deformation mechanism in annealed Cu, the dislocation-mediated plastic behavior is not observed in UFGs and NGs (Fig. 14(a) and (d)). For UFGs, the plasticity is primarily mediated by nano-twins (NTs) and stacking faults (SFs). From Fig. 14(b), the coherent NTs can be observed, and the NTs spacing ranges from 0.45 to 2 nm. At the ultrafine scale, dislocations are difficult to be traced inside the UFGs. And partial dislocations are only observed at the grain boundaries of UFGs (Fig. 14(c)). On the other hand, the increase in grain size endows NGs with dislocation storage capacity compared with UFGs. The plasticity of NGs is accommodated by partial dislocation slippage (Fig. 14(e)) and SFs (Fig. 14(f)).

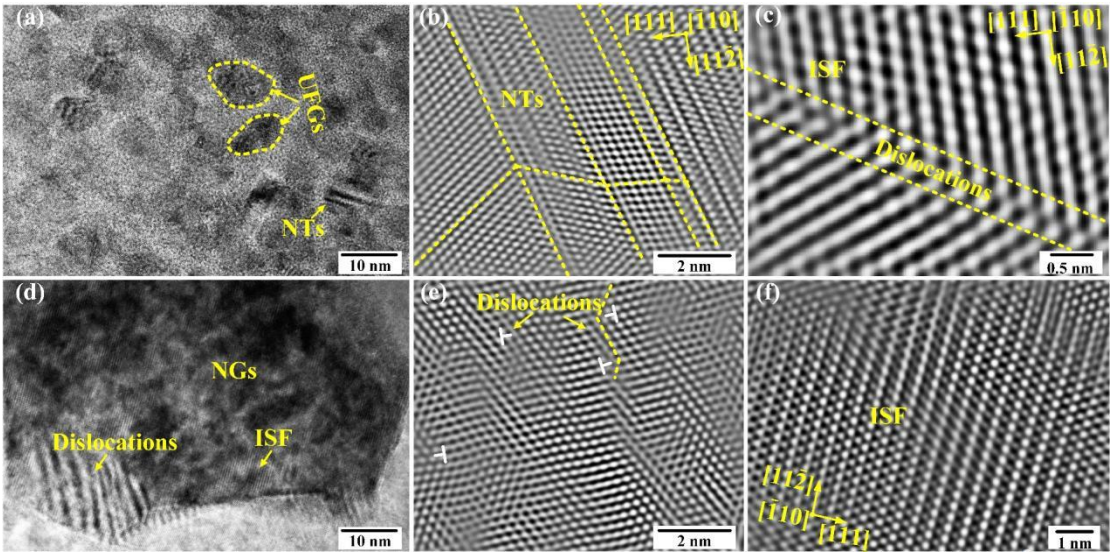

Fig. 14 The plastic mechanism of UFGs and NGs: (a) HRTEM of UFGs, (b) HRTEM of nano-twin in UFGs, (c) HRETM of the grain boundary of UFGs, (d) HRTEM of NGs, (e) HRTEM of dislocation in UFGs, (f) HRETM of the intrinsic stacking faults (ISF) of UFGs.

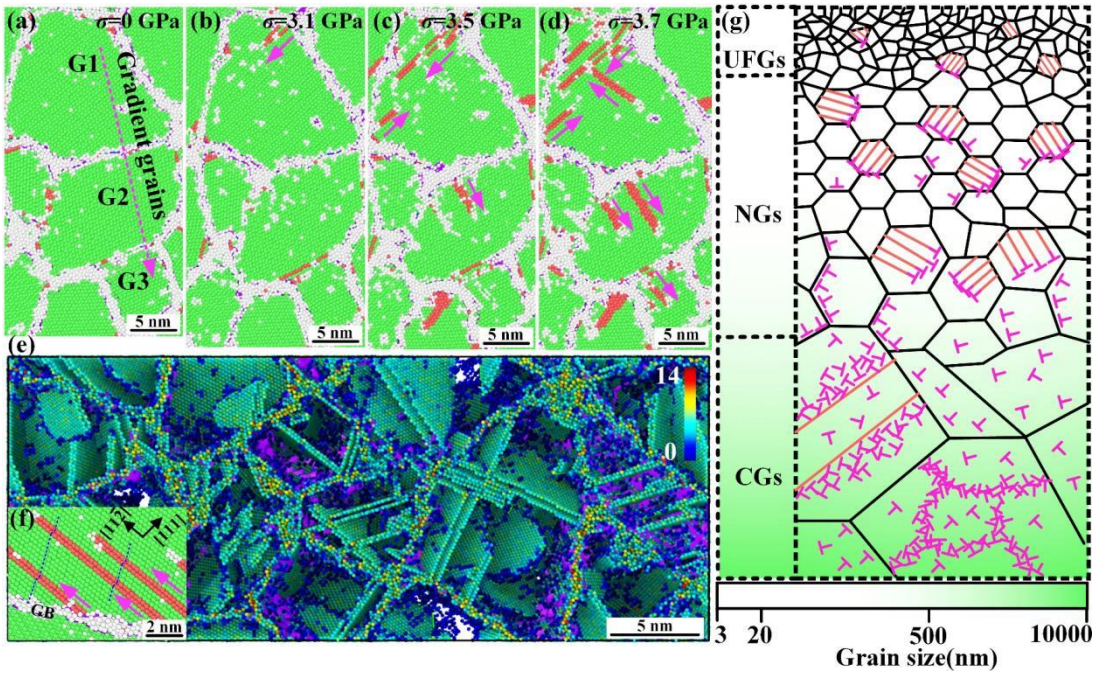

Fig. 15 MD results of the plastic deformation mechanism of the gradient grains in LSPed Cu with WDC: (a)-(d) Lattice evolution of gradient grains under different stress states, (e) 3D BTs

Preprints (www.preprints.org) | NOT PEER-REVIEWED | Posted: 4 April 2022 doi:10.20944/preprints202204.0018.v1

distribution colored with centrosymmetric parameters, (f) Orientation analysis result of NTs, (g) Schematic illustration of the multiscale plasticity mechanism in gradient grains generated by LSP with WDC.

The plasticity mechanism of the gradient NGs is further verified by MD simulations. The three grain constituting the gradient grain structure are denoted as G1, G2, and G3 (Fig. 15 (a)), and the grain sizes are ~15.2 nm, ~10.6 nm, and ~5.6 nm, respectively. The stress-strain curve obtained from the MD simulation is shown in Fig. S7. And the evolution behaviors of lattice defects of the gradient grain under different stress states are shown in Fig. 15 (b)-(d). When the stress (σ) is 3.1GPa, the ISFs are preferentially germinated in the G1. With the increase of σ (3.5 GPa), the ISF guided by partial dislocations appears in the G2. Further, the lattice defects in the G3 did not activate until the stress reached 3.7 GPa. The primary NTs in the low-strain state of the gradient grain are mainly emitted from the grain boundaries (GB), as shown in Fig. 15(e). And the orientation of the NTs (Fig. 15(f)) is consistent with the HRTEM analysis results in Fig. 14(b). The deformation and strengthening mechanism of the LSPed Cu with WDC can be described by the schematic illustration in Fig. 15(g). The gradient grains along the depth direction contribute significantly to the strength improvement of annealed Cu, which is attributed to the hidden mechanism that the lattice defects in the UFs and NGs can only be activated under high stress states. On the other hand, the plasticity of LSPed Cu is provided by the CGs in the intermediate region in the early stage of deformation, where dislocation slip and multiplication behaviors can be initiated under low stress states. On the other hand, the enhanced ductility of the LSPed Cu with WDC can be attributed to the ultra-small NTs spacing (<2 nm) in UFGs (Fig. 14(b)). It was reported that the twin spacing in Cu below 15 nm can significantly improve the ductility of UFGs, while a larger twin spacing is beneficial for strength enhancement [37,38].

In addition to the above-mentioned typical applications of the droplet-based LS process proposed in this work, other scenarios in which the process may be applied in the future are considered. Take the strain aging of 7075 Al alloy as an example. By using the LSP process with WDC at 300 ℃, the yield strength and ductility of annealed Al alloy are increased by ~87.7% and ~12%, respectively (Fig. S8 (a)). The strengthening mechanism of the Al alloy is revealed to be caused by the dynamic precipitation of nanoprecipitations [39], which is consistent with our XRD analysis results ((Fig. S8 (b))). This results demonstrate the feasibility of the application of the novel process in the field of dynamic strain aging. Further, we believe that the application of the droplet-based LS process capable of operating at high temperature can be applied to more materials with higher aging temperatures, as this process can provide a wider range of temperature options for the strain-aging of alloy materials.

4. Conclusions

Temperature-assisted laser shock process shows unique advantages in various manufacturing fields such as surface strengthening, thin-walled component forming, and micro/nano structure imprinting. Aiming at breaking the limitation of the existing confinement medium in high temperatures, we propose a novel laser shock strategy based on droplet confinement. The dynamic behaviors of droplet in laser shock process is explored. And the focusing enhancement effect of droplets of the laser beam is analyzed. By comprehensively considering the dynamic behavior and the focusing enhancement effect of droplet, the pressure calculation model of the water droplet confinement-based laser shock process is established. The effectiveness and feasibility of this process is demonstrated by the applications in laser shock forming and laser shock peening fields.

Also, the microstructure evolution and multiscale plasticity mechanisms of metal processed by laser shock with droplet confinement are studied. Major conclusions can be drawn as follows:

(1) The laser shock process based on droplet confinement can be summarized into three physical processes, which are laser-induced cavitation, laser-induced plasma and plasma confinement. The laser first excites the plasma in the droplet, and the bubbles are generated by the expansion of the plasma in the liquid. The subsequent step is the laser-induced plasma process generated by the laser irradiated on the metal target. Finally, the droplet performs the plasma confinement process accompanied by the explosion of the droplet.

(2) Droplets have a significant focusing enhancement effect. The droplet suspended on the surface of the metal target is equivalent to a liquid lens, which can refocus the laser on the near surface of the metal target. The focusing enhancement effect of the droplets exhibits a significant size-dependent effect, while the temperature and vapor layer present tiny effect on those.

(3) The droplet-based laser shock pressure primarily includes laser-induced shock wave and micro-jet shock wave. Due to the suspension characteristic and the effect of surface tension, the cavitation collapse shock wave mainly occurs above the equatorial plane of the droplets, which is different from the mechanism of the laser cavitation strengthening process based on the water layer at room temperature. And benefiting from the focusing enhancement effect of the droplet, the shock pressure is about 2.4 times higher than that of the glass confinement when the droplet confinement strategy is adopted.

(4) The laser shock process based on droplet confinement exhibits superior forming and peening effects at high temperatures. The droplet-based laser shock process can effectively induce the gradient grain structure at high temperature and achieve simultaneous improvement of the strength and ductility of the metal. Dynamic strain aging and precipitation under laser shock peening at high temperature with environmental-friendly WDC opens broad applications of the proposed strategy in the future.

Acknowledgements

This work was supported by the National Natural Science Foundation of China (Grant No. 51901162). The authors thank the support of the Chinese National Talents Program.

References

[1] M. Luo, Y. Hu, L. Hu, Z. Yao, Efficient process planning of laser peen forming for complex shaping with distributed eigen-moment, J. Mater. Process. Technol. 279 (2020) 116588. https://doi.org/10.1016/j.jmatprotec.2020.116588.

[2] H. Gao, Y. Hu, Y. Xuan, J. Li, Y. Yang, R. V. Martinez, C. Li, J. Luo, M. Qi, G.J. Cheng, Large-scale nanoshaping of ultrasmooth 3D crystalline metallic structures, Science (80-.). 346 (2014) 1352–1356. https://doi.org/10.1126/science.1260139.

[3] C.S. Montross, T. Wei, L. Ye, G. Clark, Y.W. Mai, Laser shock processing and its effects on microstructure and properties of metal alloys: A review, Int. J. Fatigue. 24 (2002) 1021–1036. https://doi.org/10.1016/S0142-1123(02)00022-1.

[4] Y. Liao, C. Ye, G.J. Cheng, [INVITED] A review: Warm laser shock peening and related laser processing technique, Opt. Laser Technol. 78 (2016) 15–24. https://doi.org/10.1016/j.optlastec.2015.09.014.

[5] J. Man, J. Zhao, H. Yang, L. Song, D. Liu, Study on laser shock imprinting nanoscale line textures on metallic foil and its application in nanotribology, Mater. Des. 193 (2020) 108822.

https://doi.org/10.1016/j.matdes.2020.108822.

[6] Y. Haifeng, X. Fei, W. Yan, J. Le, L. Hao, H. Jingbin, Manufacturing profile-free copper foil using laser shock flattening, Int. J. Mach. Tools Manuf. 152 (2020) 103542. https://doi.org/10.1016/j.ijmachtools.2020.103542.

[7] P. Kumar, J. Liu, M. Motlag, L. Tong, Y. Hu, X. Huang, A. Bandopadhyay, S.K. Pati, L. Ye, J. Irudayaraj, G.J. Cheng, Laser Shock Tuning Dynamic Interlayer Coupling in Graphene-Boron Nitride Moir é Superlattices, Nano Lett. 19 (2019) 283–291. https://doi.org/10.1021/acs.nanolett.8b03895.

[8] Y. Hu, Y. Xuan, X. Wang, B. Deng, M. Saei, S. Jin, J. Irudayaraj, G.J. Cheng, Superplastic Formation of Metal Nanostructure Arrays with Ultrafine Gaps, Adv. Mater. 28 (2016) 9152–9162. https://doi.org/10.1002/adma.201602497.

[9] Y. Haifeng, X. Fei, L. Kun, M. Jiaxiang, C. Haoxue, L. Hao, H. Jingbin, Research on temperature-assisted laser shock imprinting and forming stability, Opt. Lasers Eng. 114 (2019) 95–103. https://doi.org/10.1016/j.optlaseng.2018.11.002.

[10] W. Zhou, J. Lin, D.S. Balint, T.A. Dean, Clarification of the effect of temperature and strain rate on workpiece deformation behaviour in metal forming processes, Int. J. Mach. Tools Manuf. 171 (2021) 103815. https://doi.org/10.1016/j.ijmachtools.2021.103815.

[11] X. Pan, X. Wang, Z. Tian, W. He, X. Shi, P. Chen, L. Zhou, Effect of dynamic recrystallization on texture orientation and grain refinement of Ti6Al4V titanium alloy subjected to laser shock peening, J. Alloys Compd. 850 (2021) 156672. https://doi.org/10.1016/j.jallcom.2020.156672.

[12] P. Shukla, R. Crookes, H. Wu, Shock-wave induced compressive stress on alumina ceramics by laser peening, Mater. Des. 167 (2019) 107626. https://doi.org/10.1016/j.matdes.2019.107626.

[13] D.C. van Aswegen, C. Polese, Experimental and analytical investigation of the effects of laser shock peening processing strategy on fatigue crack growth in thin 2024 aluminium alloy panels, Int. J. Fatigue. 142 (2021) 105969. https://doi.org/10.1016/j.ijfatigue.2020.105969.

[14] X. Zheng, P. Luo, G. Yue, Y. Hu, Analysis of microstructure and high-temperature tensile properties of 2060 Al-Li alloy strengthened by laser shock peening, J. Alloys Compd. 860 (2021) 158539. https://doi.org/10.1016/j.jallcom.2020.158539.

[15] A.G. Sanchez, C. You, M. Leering, D. Glaser, D. Furfari, M.E. Fitzpatrick, J. Wharton, P.A.S. Reed, Effects of laser shock peening on the mechanisms of fatigue short crack initiation and propagation of AA7075-T651, Int. J. Fatigue. 143 (2021) 106025. https://doi.org/10.1016/j.ijfatigue.2020.106025.

[16] C. Ye, S. Suslov, B.J. Kim, E.A. Stach, G.J. Cheng, Fatigue performance improvement in AISI 4140 steel by dynamic strain aging and dynamic precipitation during warm laser shock peening, Acta Mater. 59 (2011) 1014–1025. https://doi.org/10.1016/j.actamat.2010.10.032.

[17] C. Ye, Y. Liao, S. Suslov, D. Lin, G.J. Cheng, Ultrahigh dense and gradient nano-precipitates generated by warm laser shock peening for combination of high strength and ductility, Mater. Sci. Eng. A. 609 (2014) 195–203. https://doi.org/10.1016/j.msea.2014.05.003.

[18] W. Li, H. Chen, W. Huang, J. Chen, L. Zuo, C. Li, J. He, Y. Ren, S. Zhang, Effect of laser shock peening on high cycle fatigue properties of aluminized AISI 321 stainless steel, Int. J. Fatigue. 147 (2021) 106180. https://doi.org/10.1016/j.ijfatigue.2021.106180.

[19] L. Kun, Y. Haifeng, X. Fei, M. Jiaxiang, C. Haoxue, Research on the dynamic yield strength and forming depth of microscale laser shock imprinting, Opt. Laser Technol. 116 (2019) 189–

195. https://doi.org/10.1016/j.optlastec.2019.03.026.

[20] D. Jang, J.H. Oh, J.M. Lee, D. Kim, Enhanced efficiency of laser shock cleaning process by geometrical confinement of laser-induced plasma, J. Appl. Phys. 106 (2009) 14913. https://doi.org/10.1063/1.3160315.

[21] M. Duocastella, C. Florian, P. Serra, A. Diaspro, Sub-wavelength Laser Nanopatterning using Droplet Lenses, Sci. Rep. 5 (2015) 16199. https://doi.org/10.1038/srep16199.

[22] B. Banerjee, An evaluation of plastic flow stress models for the simulation of high-temperature and high-strain-rate deformation of metals, 2005.

[23] S. Plimpton, Fast Parallel Algorithms for Short-Range Molecular Dynamics, J. Comput. Phys. 117 (1995) 1–19.

[24] X.W. Zhou, H.N.G. Wadley, R.A. Johnson, D.J. Larson, N. Tabat, A. Cerezo, A.K. Petford-Long, G.D.W. Smith, P.H. Clifton, R.L. Martens, T.F. Kelly, Atomic scale structure of sputtered metal multilayers, Acta Mater. 49 (2001) 4005–4015. https://doi.org/10.1016/S1359-6454(01)00287-7.

[25] M. Gradeck, N. Seiler, P. Ruyer, D. Maillet, Heat transfer for Leidenfrost drops bouncing onto a hot surface, Exp. Therm. Fluid Sci. 47 (2013) 14–25. https://doi.org/10.1016/j.expthermflusci.2012.10.023.

[26] G.E. Cossali, M. Marengo, M. Santini, Secondary atomisation produced by single drop vertical impacts onto heated surfaces, Exp. Therm. Fluid Sci. 29 (2005) 937–946. https://doi.org/10.1016/j.expthermflusci.2004.12.003.

[27] L.M. Cabal ín, A. Gonz ález, V. Lazic, J.J. Laserna, Laser-induced breakdown spectroscopy of metals covered by water droplets, Spectrochim. Acta - Part B At. Spectrosc. 74–75 (2012) 95–102. https://doi.org/10.1016/j.sab.2012.06.038.

[28] A. Patrascioiu, J.M. Fern ández-Pradas, A. Palla-Papavlu, J.L. Morenza, P. Serra, Laser-generated liquid microjets: Correlation between bubble dynamics and liquid ejection, Microfluid. Nanofluidics. 16 (2014) 55–63. https://doi.org/10.1007/s10404-013-1218-5.

[29] H. Zhang, Z. Lu, P. Zhang, J. Gu, C. Luo, Y. Tong, X. Ren, Experimental and numerical investigation of bubble oscillation and jet impact near a solid boundary, Opt. Laser Technol. 138 (2021) 106606. https://doi.org/10.1016/j.optlastec.2020.106606.

[30] A.L. Biance, C. Clanet, D. Qu ér é, Leidenfrost drops, Phys. Fluids. 15 (2003) 1632–1637. https://doi.org/10.1063/1.1572161.

[31] T. Požar, V. Agrež, R. Petkovšek, Laser-induced cavitation bubbles and shock waves in water near a concave surface, Ultrason. Sonochem. 73 (2021) https://doi.org/10.1016/j.ultsonch.2020.105456.

[32] J. Gu, C. Luo, Z. Lu, P. Ma, X. Xu, X. Ren, Bubble dynamic evolution, material strengthening and chemical effect induced by laser cavitation peening, Ultrason. Sonochem. 72 (2021) 105441. https://doi.org/10.1016/j.ultsonch.2020.105441.

[33] E.A. Brujan, T. Ikeda, Y. Matsumoto, On the pressure of cavitation bubbles, Exp. Therm. Fluid Sci. 32 (2008) 1188–1191. https://doi.org/10.1016/j.expthermflusci.2008.01.006.

[34] M. Srivastava, S. Hloch, L. Krejci, S. Chattopadhyaya, N. Gubeljak, M. Milkovic, Utilizing the water hammer effect to enhance the mechanical properties of AISI 304 welded joints, Int. J. Adv. Manuf. Technol. 119 (2022) 2317–2328. https://doi.org/10.1007/s00170-021-08357-9.

[35] R. Fabbro, J. Fournier, P. Ballard, D. Devaux, J. Virmont, Physical study of laser-produced plasma in confined geometry, J. Appl. Phys. 68 (1990) 775–784.

 doi:10.20944/preprints202204.0018.v1

https://doi.org/10.1063/1.346783.

[36] L. Berthe, R. Fabbro, P. Peyre, L. Tollier, E. Bartnicki, Shock waves from a water-confined laser-generated plasma ARTICLES YOU MAY BE INTERESTED IN, J. Appl. Phys. 82 (1997) 2826. https://doi.org/10.1063/1.366113.

[37] L. Lu, X. Chen, X. Huang, K. Lu, Revealing the maximum strength in nanotwinned copper, Science (80-.). 323 (2009) 607–610. https://doi.org/10.1126/science.1167641.

[38] L. Lu, M.L. Sui, K. Lu, Superplastic extensibility of nanocrystalline copper at room temperature, Science (80-.). 287 (2000) 1463–1466. https://doi.org/10.1126/science.287.5457.1463.

[39] C. Ye, Y. Liao, S. Suslov, D. Lin, G.J. Cheng, Ultrahigh dense and gradient nano-precipitates generated by warm laser shock peening for combination of high strength and ductility, Mater. Sci. Eng. A. 609 (2014) 195–203. https://doi.org/10.1016/j.msea.2014.05.003.